

# Gaussian beam profile effectiveness on double rephasing photon echoes

Byoung S. Ham

Center for Photon Information Processing, and School of Electrical Engineering and Computer Science,  
Gwangju Institute of Science and Technology

123 Chumdangwagi-ro, Buk-gu, Gwangju 61005, S. Korea

bham@gist.ac.kr

(January 16, 2017)

**Abstract:** Over the last decade, photon echoes have been intensively studied as a potential candidate of quantum memories owing to the inherent benefits of ultrafast, wide bandwidth, and multi-mode information processing capabilities. The key mechanism of photon echoes is in the rephasing of coherence evolutions of inhomogeneously broadened ensemble atoms. This allows for the reversible information processing which in turn satisfies unitarity in quantum mechanics. Even in an ideal system, however, the echo efficiency can be degraded due to imperfect retrieval processes when commercial laser light is directly used due to its Gaussian distribution in space. Although the fidelity of quantum memory has nothing to do with the retrieval efficiency, its practicality in quantum information relies on a near perfect efficiency to avoid potential eavesdropping by the device-dependent loopholes in quantum cryptography or to reduce ancilla qubits in fault-tolerant quantum computing. Here the Gaussian light-dependent photon echo efficiency is numerically analyzed and discussed for the recently observed unpermitted photon echoes in various experiments to support quantum coherence control in photon echoes.

## Introduction

Quantum memory [1-9] has become an emerging research topic of quantum information recently faced with serious challenges regarding qubit scalability [10] due mainly to the short decoherence time of qubits. The qubit scalability plays an important role not only for quantum algorithms such as Shor's prime number factorization [11] and Grover's data search [12], but also for fault-tolerant quantum computers [13] and quantum repeaters [14]. Photon echoes [15,16], intensively studied in the 1980s and 1990s with benefits of broadband ultrafast all-optical information capabilities, have now been applied for quantum memories with additional benefits of multimode accessibility and complete absorption [1-6]. The beauty of photon echo-based quantum memories is in the classical controllability of random coherence of inhomogeneously broadened ensemble atoms (ions or spins), where a  $\pi$ -optical pulse makes the direction of coherence evolution in a two-level system reversed. Thus, the stored quantum optical information can be perfectly retrieved even when the macroscopic ensemble coherence completely fades out. This means that the resonant optical  $\pi$ -pulse implies classical controllability (reversibility) for the quantum coherence evolutions of ensemble atoms. The disordered ensemble system in coherence turns out to be ordered reversibly and symmetrically in time domain, without violating the entropy theory of thermodynamics owing to the enforced energy inflow into the system.

The reversible coherence evolution in photon echoes relies on a population inversion-incurred  $\pi$ -phase shift by a  $\pi$ -optical pulse, resulting in intrinsic quantum noises due to either spontaneous or stimulated emissions. Unlike classical information processing, quantum information

does not allow amplification (or cloning) of an unknown quantum state [17]. Thus, photon echo itself has had a severe constraint for quantum memory applications. Over the last decade avoiding the population inversion in photon echoes has been the main problem to solve [1-7]. In 2000s, the ensemble rephasing without population inversion has been achieved by using either counter-propagating optical pulses [1] or polarity reversible dc electric fields [5]: Controlled reversible inhomogeneous broadening (CRIB). Although the CRIB techniques have been successful in overcoming the population inversion constraint in photon echoes, a short storage time still limits the qubit scalability in both measurement-based quantum computing [18] and quantum repeater-based long-distance quantum communications [19]. Thus, the storage time extension has become another issue to pursue in photon echo-based quantum memories.

Double rephasing photon echoes have been studied recently for quantum memories due to the inherent property of no population inversion. Although the first echo in the double rephasing photon echo scheme has been treated well not to rephase macroscopically to avoid any affection on the second (final) echo [20,21], the absorptive coherence of the second echo cannot, in principle, contribute to echo emission (i.e. radiation). This issue has originally been discussed in the controlled double rephasing (CDR) echoes by combining it with a quantum coherence control via Rabi flopping to a third (spin) state [22,23]. The Rabi flopping in CDR echoes inverts the system coherence by converting the optical coherence into spin coherence and vice versa [24]. This coherence inversion is the key mechanism of quantum coherence in CDR echoes to convert the absorptive photon echo into an emissive one in the double rephasing scheme. Thus, the CDR echo becomes a storage time-extended quantum memory protocol simply because the spin coherence decay time is much longer than the photon echo decay time. Surprisingly double rephasing photon echoes without the control pulse have been recently observed [20,21], which should seemingly contradict the CDR echo theory [23]. Here, we numerically prove that the echo observations in the bare double rephasing schemes are neither an artifact of, nor a contradiction to, CDR echoes. Moreover we numerically demonstrate that the unpermitted photon echo observations always exist regardless of the rephasing pulse area due to Gaussian distribution of light pulses in a transverse mode.

## Methods

Due to the Gaussian beam profile  $G_j$  of commercial laser light, all kinds of pulse areas ( $\sum \Phi_j$ ) can be generated by a single light pulse interacting with an ensemble:  $\Phi_j = \int_0^T \Omega_j dt \cong \Omega_j T$ . Here, the Rabi frequency  $\Omega_j$  depends only on  $G_j$ , where  $j$  is the position along the transverse direction with respect to the pulse propagation direction, and  $T$  is the time duration of a square pulse which can be easily obtained with modern electro-optic devices. To check whether the echo observations in the double rephasing schemes [20,21] contradict CDR echoes or not, we calculate all individual atoms' coherence evolutions allocated to all components of the Gaussian distributed light. We do not consider axial distribution of the pulse, which deals with Maxwell-Bloch equations. For the interacting ensemble we set zero decay rates for perfect reversibility. Then, the system's coherence becomes functions of both optical inhomogeneous broadening and the spatial (Gaussian) distribution of the interacting pulses.

For the numerical calculations time-dependent density matrix equations are solved in an interacting Heisenberg picture under rotating wave approximations [25]:  $\frac{d\rho}{dt} = \frac{i}{\hbar} [H, \rho] - \frac{1}{2} \{\Gamma, \rho\}$ , where  $\rho$  is density matrix elements,  $H$  is Hamiltonian, and  $\Gamma$  is decay parameters. For this a commercial laser light whose spatial profile is Gaussian distributed is taken as a light source. The Gaussian profile is divided into 41 subgroups (otherwise specified), where it covers 99.55% of the total area. Each subdivision of Gaussian light-corresponding atoms is divided into 281 spectral groups

at 10 Hz spacing for the 1.2 MHz (FWHM) inhomogeneous broadening. Those 281 spectral groups are individually calculated and summed across each spatial component of the Gaussian distributed atom groups. The Gaussian light-corresponding atom groups do not overlap (or interact) with each other, resulting in no interference among them due to transverse (spatial) distribution. Photon echoes exactly satisfy phase matching conditions in nonlinear optics:  $\mathbf{k}_{echo} = 2\mathbf{k}_{rephasing} - \mathbf{k}_{data}$ . Thus, only the emissive components of photon echoes contribute to the final echo radiation (or emission). The optical pulse duration is set at 0.1  $\mu\text{s}$ , and the time increment in the calculations is 0.01  $\mu\text{s}$ . Initially all atoms are in the ground state  $|1\rangle$  ( $\rho_{11} = 1$ ), and all coherence is  $\rho_{ij} = 0$ , where  $i$  ( $j$ )=1 and 2. The program used for the simulations is time-interval independent, so that there is no accumulated error dependent on the time interval setting. For a  $\pi$  pulse area the corresponding Rabi frequency of the pulse is 5 MHz. Here, the pulse area is related with only the varying Rabi frequency, e.g., in the Gaussian spatial distribution.

## Results and Discussion

Figure 1 shows the two-pulse photon echo simulation, where the light pulse(s) has a Gaussian distribution in a transverse direction. The spatial shape of the light pulse perfectly maps onto a cross section of the interacting ensemble medium, resulting in spatially distributed independent atoms. For simplicity of symmetry, we take only one-dimensional transverse mode of the cross section. For better analysis of the Gaussian pulse-dependent photon echoes, three combinations of the Gaussian pulse(s) are used: The first column in Fig. 1 is the Gaussian pulse with data (D) only; The second column is for the Gaussian pulse with rephasing (R) only; The third column is for all Gaussian pulses. The first row of the panel shows the shape and sequence of the pulse for the three different cases. The second row shows the corresponding simulation results of the first row, where the complete rephasing appears at  $t=4.1 \mu\text{s}$  (dotted line). The third row shows the peak amplitude (red marks) of the photon echoes in the second row along the dotted line, and the solid line represents the best-fit curve.

For the case of data only Gaussian spatial distribution in the first column, the echo perfectly fits the function of  $\sin(G_j)$ , where  $G_j$  is the pulse area at each point of the Gaussian profile. This exactly mimics the area theorem of photon echoes [26,27], where the  $\pi$  optical pulse perfectly rephases all of the data components. Although the area theorem originates in the time domain, the echo efficiency  $\eta$  reaches 100% as shown in the lower left corner (see the [Supplementary information Figure 1](#)). Here, the data pulse-induced coherence profile overlaps with the echo profile. For the case of rephasing-only Gaussian pulse in the second column, the best-fit curve is  $\sin^2(G_j)$ . Because the rephasing pulse area is twice of the area represented by the data ( $\mathbf{k}_{echo} = 2\mathbf{k}_{rephasing} - \mathbf{k}_{data}$ ), the square dependence law can be accepted. Here all echo efficiencies are lower than unity except for the ideal  $\pi/2-\pi$  pulse sequence at center of  $G_j$ . The resulting echo efficiency is about 50%. In fact, the echo area in the second column is 79% with respect to the data pulse area in the first column. For the last case of more general situations in the third column, the echo distribution profile is shrunken narrower than that of the data (dotted curve), and the echo efficiency drops down to  $\sim 70\%$ . Interestingly the best-fit curve is  $\sin^3(G_j)$ , which is the product of the first and second cases. Here, the Gaussian pulse induces 30% retrieval leakage due to imperfect rephasing process, and this leakage may allow unpermitted echo generations in the double rephasing photon echoes (will be discussed in Figs. 2 and 3).

Now let's consider the double rephasing photon echoes observed recently in modified photon echo quantum memories, where the first echo is erased macroscopically not to affect the second echo [20,21]. Figure 2(a) shows a typical pulse sequence of the double rephasing photon echoes composed of  $\pi-\pi$  rephasing pulse sequence. As discussed in refs. 22-24, the second echo must not be irradiated

from the medium due to its absorptive characteristics. To make it irradiative, a control Rabi pulse must be inserted as discussed in CDR echoes [22,23]. Thus, we need to analyze how the doubly rephased photon echoes in refs. 20 and 21 are possible. Figure 2 shows double rephasing photon echo results, where identical rephasing pulses R1 and R2 are applied consecutively after the data pulse D. For the analysis, the rephasing pulses (R1 and R2) are set to vary linearly from zero to  $2\pi$  (10 MHz) in pulse area (Rabi) for the identical  $\pi/2$  data pulse D. The linear spatial distribution of the rephasing pulses is shown in Fig. 2(b).

Figures 2(c) and 2(d) represent corresponding numerical simulations for Figs. 2(a) and 2(b), where emissive photon echoes are generated when the rephasing pulse area falls near  $\pi/2$  and  $3\pi/2$  (see E2 for the yellow region in Fig. 2(c)). This is due to the imperfect rephasing by R1 as discussed in Fig. 1. Figure 2(e) is the plot of echo amplitudes in Fig. 2(c) as a function of the rephasing pulse area in Fig. 2(b), where echo E2 (red circles) has a certain portion of emissive components ( $Im\rho_{12}>0$ ). The emissive photon echo regions are repeated at every rephasing pulse area,  $\Phi = 2n\pi[-\alpha, \alpha]$ , where  $\alpha \cong 5\pi/8$  (see also the Supplementary Figure 2). Each solid curve represents the best-fit curve for Fig. 2(c), and echo coherence amplitudes of E1 and E2 are denoted by:

$$E1 = \sin^2\left(\frac{\Phi}{2}\right)/2, \quad (1)$$

$$E2 = -\sqrt{2}\left[\sin^2\left(\frac{\Phi}{2}\right)[0.3 - \cos^2\left(\frac{\Phi}{2}\right)]\right], \quad (2)$$

where E1 has the same form as the second case (second column) in Fig. 1. Here the assumption of the silent echo for E1 does not change the generality of the present analysis, because the silence does not alter individual coherence evolutions [20]. Thus, we conclude that the final echo E2 can be generated due to the imperfect rephasing pulse area applied to the double rephasing scheme. As a result, the echo observations in the double rephasing photon echo experiments in refs. 20 and 21 are real and do not contradict the CDR echo theory [23]. Figure 2(f) shows all components of the final echo E2 in time domain. The majority of absorptive echo components in Fig. 2(f) is simply reabsorbed by the medium, and has no influence to the emissive echo components due to spatial independence.

Figure 3 shows the practical case of the double rephasing photon echoes, where all the light pulses interacting with a medium are Gaussian distributed along the transverse direction with respect to the beam propagation direction as shown in Figs. 3(a) and (b). The data pulse area is set at  $\pi/5$ . The red circles in Fig. 3(a) indicate the values calculated by Eq. (2) for  $E2=0$ . Figures 3(c) and 3(d) show the results of individual coherence evolutions for Fig. 3(b). Unlike the theory discussed in the CDR echoes, the second echo E2 shows partially emissive components at the sidebands near  $\frac{(2n-1)\pi}{2}$  pulse area satisfying Eq. (2). In Fig. 3(e), the first echo E1 at  $t=6.1 \mu\text{s}$ , and the second echo E2 at  $t=12.1 \mu\text{s}$  are extracted. The red curve represents only for the emissive components  $E2_{\text{eff}}$ , selected from the second echo E2 represented by the dashed curve. The emissive region of  $E2_{\text{eff}}$  also satisfies  $\Phi = 2n\pi[-\alpha, \alpha]$  at  $\alpha \cong 5\pi/8$  in Eq. (2). Figure 3(f) shows the coherence sum of the red curve in Fig. 3(e) in time domain for all spatial components in Fig. 3(c), where Fig. 3(g) shows all spatial components of it. The echo efficiency of  $E2_{\text{eff}}$  in Fig. 3(f) is calculated at 6.9 % of the data pulse-induced coherence.

Figure 3(h) is the summary of echo  $E2_{\text{eff}}$  efficiency for different cases of Fig. 3(b), where the peak pulse amplitude (pulse area) of the Gaussian profile varies from zero to  $2\pi$  at a  $\pi/4$  step (see also the Supplementary Figure 3). As shown in Fig. 3(h), the emissive echo efficiency  $E2_{\text{eff}}$  shows a damped oscillation. The damping is due to inhomogeneously broadened atoms as discussed in ref. 28.

From Fig. 3(h), it is concluded that the unpermitted photon echo E2 in the double rephasing scheme always exists regardless of the rephasing pulse area if the light pulses are Gaussian distributed. The maximum efficiency of 26% is achieved with  $\pi/2$  rephasing pulse area. More importantly the echo efficiency  $E_{2\text{eff}}$  converges at  $\sim 10\%$  as the rephasing pulse area increases (see the best-fit curve). This clearly explains how echo observations in the double rephasing photon echo schemes in refs. 20 and 21 were possible, showing that it is neither an artifact nor a contradiction to the CDR echoes. This impossible echo generation in Fig. 3(h), however, is also understood as a coherence leakage due to imperfect rephasing. Thus, the double rephasing photon echo scheme itself cannot be used for practical quantum memory applications due to too weak echo efficiency. For a near maximal echo efficiency, not only adding a control Rabi pulse as shown in the CDR echoes, but also a flattened rephasing pulse shaping is required as shown in Fig. 1.

## Conclusion

In conclusion, double rephasing photon echoes were numerically analyzed for Gaussian pulse effectiveness. The echo observations in the bare double rephasing photon echo schemes [20,21] are neither an artifact nor contradiction to the CDR echo theory [23]. Instead, they were due to the imperfect rephasing process by Gaussian pulses, and the related formula was induced. As a result there were always positive echo generations regardless of the rephasing pulse area. The resultant echo efficiency showed a damped oscillation converging at  $\sim 10\%$ . The Gaussian pulse spatial distribution also implies a coherence leakage in rephasing processes. Considering potential eavesdropping in quantum channels due to device imperfectness-caused loopholes [29] and errors accumulated in each gate operations for error-corrections [30] in fault-tolerant quantum computing [13,30], keeping near perfect retrieval efficiency is important. Thus, the spatial profile of the rephasing pulses must be made flat to minimize the coherence leakage and to satisfy a near perfect echo efficiency for quantum memory applications, such as entanglement swapping for qubit (or quantum node) scalability [19,31].

## Acknowledgment

This work was supported by ICT R&D program of MSIP/IITP (1711028311: Reliable crypto-system standards and core technology development for secure quantum key distribution network).

## References

1. S. A. Moiseev and S. Kröll, Phys. Rev. Lett. **87**, 173601 (2001).
2. A. I. Lvovsky, B. C. Sanders, and W. Tittel, Nature Photon. **3**, 706 (2009).
3. H. de Riedmatten, M. Afzelius, M. U. Staudt, C. Simon, and N. Gisin, Nature **456**, 773 (2008).
4. W. Tittel, M. Afzelius, T. Chanelière, R. L. Cone, S. Kröll, S. A. Moiseev, and M. Sellars, Laser & Photon. Rev. **4**, 244 (2010).
5. G. Hetet, J. J. Longdell, A. L. Alexander, P. K. Lam, and M. J. Sellars, Phys. Rev. Lett. **100**, 023601 (2008).
6. B. S. Ham, Phys. Rev. A **85**, 031402(R) (2012); *ibid*, Phys. Rev. A **94**, 049905(E) (2016).
7. E. Saglamyurek, E. Saglamyurek, N. Sinclair, J. Jin, J. A. Slater, D. Oblak, F. Bussi eres, M. George, R. Ricken, W. Sohler, and W. Tittel, Nature **469**, 512 (2011).
8. B. Julsgaard, C. Grezes, P. Bertet, K. M olmer, Phys. Rev. Lett. **110**, 250503 (2013).
9. P. C. Maurer, G. Kucsko, C. Latta, L. Jiang, N. Y. Yao, S. D. Bennett, F. Pastawski, D. Hunger, N. Chisholm, M. Markham, D. J. Twitchen, J. I. Cirac, and M. D. Lukin, Science; **336**, 1283 (2012).
10. T. Monz, P. Schindler, J. T. Barreiro, M. Chwalla, D. Nigg, W. A. Coish, M. Harlander, W. H ansel, M. Hennrich, and R. Blatt, Phys. Rev. Lett. **106**, 130506 (2011).

11. L. M. K. Vandersypen, M. Steffen, G. Breyta, C. S. Yannoni, M. H. Sherwood, and I. L. Chuang, *Nature* **414**, 883 (2001), and references therein.
12. L. K. Grover, "A *fast quantum mechanical algorithm for database search*," Proceedings, 28th Annual ACM Symposium on the Theory of Computing, p. 212 (May 1996).
13. A. M. Steane, *Nature* **399**, 124 (1999).
14. L.-M. Duan, M. D. Lukin, J. I. Cirac & P. Zoller, *Nature* **414**, 413 (2001).
15. N. A. Kurnit, I. D. Abella, and S. R. Hartmann, *Phys. Rev. Lett.* **13**, 567 (1964).
16. T. W. Mossberg, *Opt. Lett.* **7**, 77 (1982).
17. W. K. Wootters and W. H. Zurek, *Nature* **299**, 802 (1982).
18. R. Raussendorf and H. J. Briegel, *Phys. Rev. Lett.* **86**, 5188 (2001).
19. I. Usmani, C. Clausen, F. Bussières, N. Sangouard, M. Afzelius, and N. Gisin, *Nature Photon.* **6**, 234 (2012).
20. V. Damon, M. Bonarota, A. Louchet-Chauvet, T. Chanelière, and J. L. Le Gouët, *New. J. Phys.* **13**, 093031 (2011).
21. A. Arcangeli, A. Ferrier, and Ph. Goldner, *Phys. Rev. A* **93**, 062303 (2016).
22. B. S. Ham, "Atom phase controlled noise-free photon echoes," arXiv:1101.5480.
23. B. S. Ham, "Collective atom phase controls in photon echoes for quantum memory applications I: Population inversion removal," arXiv:1612.0115v2
24. B. S. Ham, *Opt. Exp.* **18**, 1704 (2010).
25. M. Sargent III, M. O. Scully, W. E. Lamb Jr., *Laser Physics*, Addison-Wesley (1974).
26. S. L. McCall and E. L. Hahn, *Phys. Rev.* **183**, 457 (1969).
27. E. L. Hahn, N. S. Shiren, and S. L. McCall, *Phys. Lett.* **37A**, 256 (1971).
28. B. S. Ham, "A controlled ac Stark echo for quantum memories," arXiv:1612.02193
29. H.-K. Lo, M. Curty, and B. Qi, *Phys. Rev. Lett.* **108**, 130503 (2012).
30. J. Preskill, *Phys. Today* (June 1999).
31. L. Li, Y. O. Dudin, and A. Kuzmich, *Nature* **498**, 466 (2013).

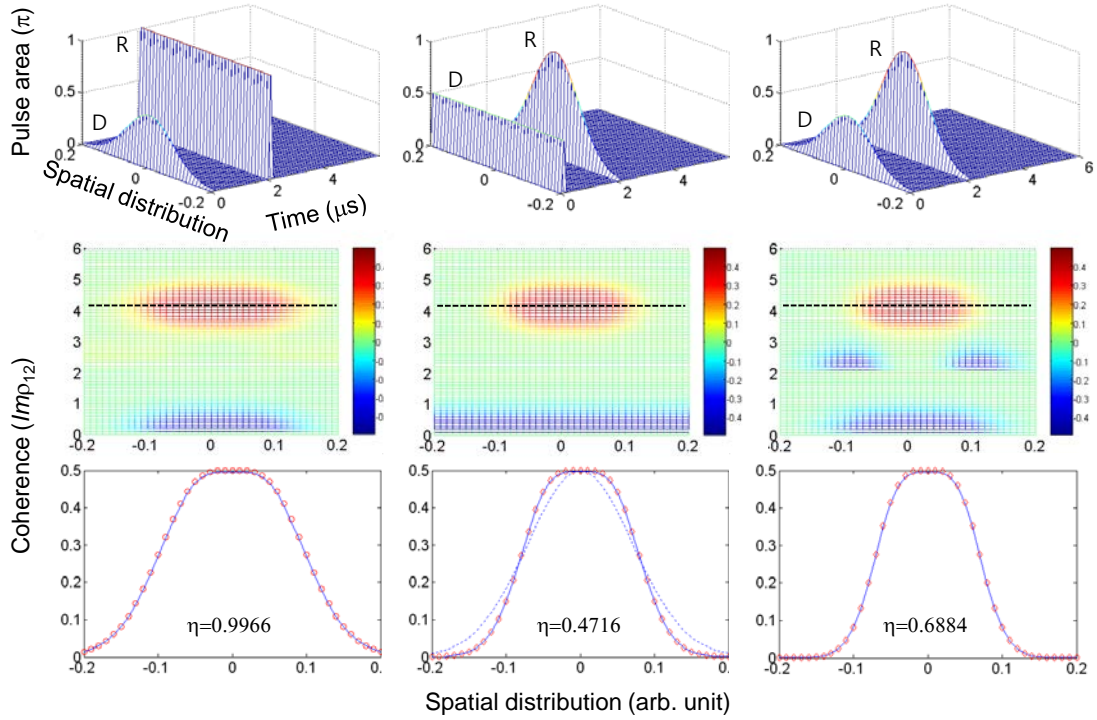


FIG. 1. Gaussian pulse dependent two-pulse photon echo efficiency. First row: three-different pulse shapes; Second row: Corresponding coherence as functions of time and pulse distribution; Third row: Corresponding echo profile and its best-fit curve along the dotted line in the second row; The data (D;  $t=0.1 \mu\text{s}$ ) and rephasing (R;  $t=2.1 \mu\text{s}$ ) pulses have Gaussian distribution. The Gaussian distribution is along the transverse direction, the optical power of 5 (10) MHz corresponds to the area of  $\pi/2$  ( $\pi$ ). The pulse duration of each pulse is set by  $0.1 \mu\text{s}$ . The spatial distribution of each pulse is divided into 41 sections for calculations. The blue curve in the bottom row indicates a theoretical fit, where the red marks are for the average of  $Imp_{12}$  (photon echo) at  $t=4.1 \mu\text{s}$  along the dotted line in the middle row. From left to right, the theoretical fit is for  $\sin(G)$ ,  $\sin^2(G)$ , and  $\sin^3(G)$ , where  $G$  is the Gaussian distribution. Dotted curve: the Gaussian profile. The echo efficiency  $\eta$  is defined by  $\eta = \frac{|\sum_j \rho_{12}(t_e)|}{|\sum_j \rho_{12}(t_d)|}$ , where  $j$  is the Gaussian distribution and  $t_d$  and  $t_e$  is the data and echo time.

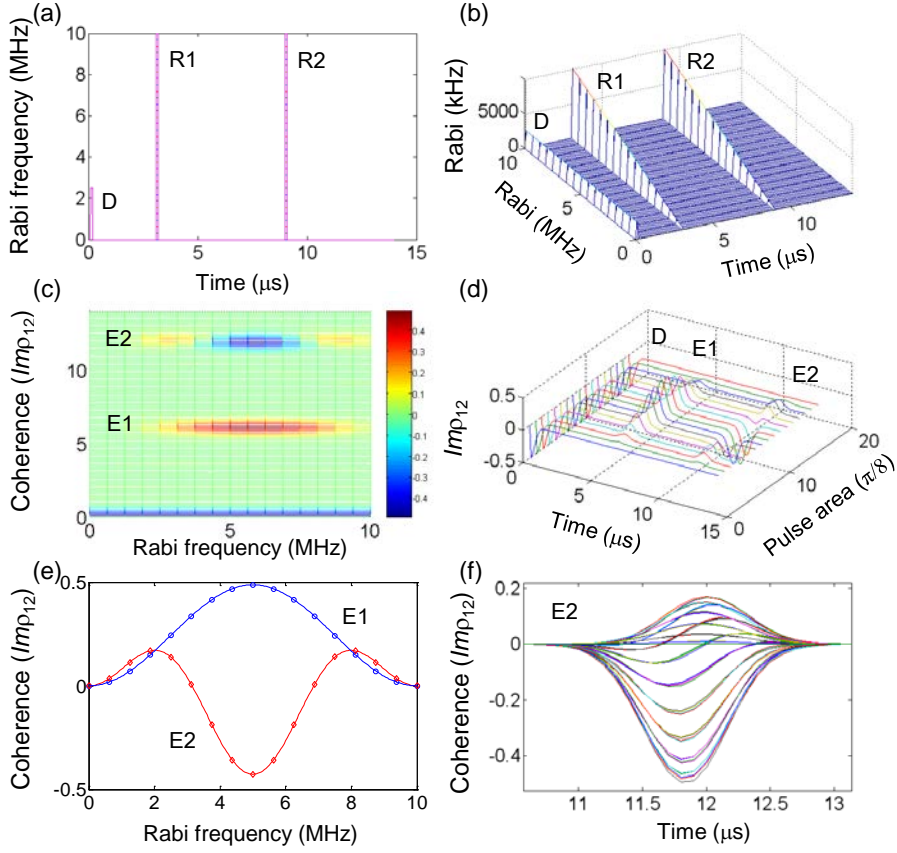


Figure 2. Photon echoes for linearly varying rephasing Rabi frequency. (a) Pulse sequence for the double rephasing photon echo. D: Data pulse ( $\pi/2$ ); R1: First rephasing pulse; R2: Second rephasing pulse (b) Rephasing Rabi frequencies for (a). (c) Optical coherence for each Rabi frequency of (b). E1 (E2) indicates the first (second) echo. (d) Individual atom phase evolution for (c). (e) Photon echo efficiency for the first echo E1 (blue diamond) and the second echo E2 (red circle): Eqs. (1) and (2). Each colored curve is for the best-fit curve (text). (f) All cases of E2 in (c).

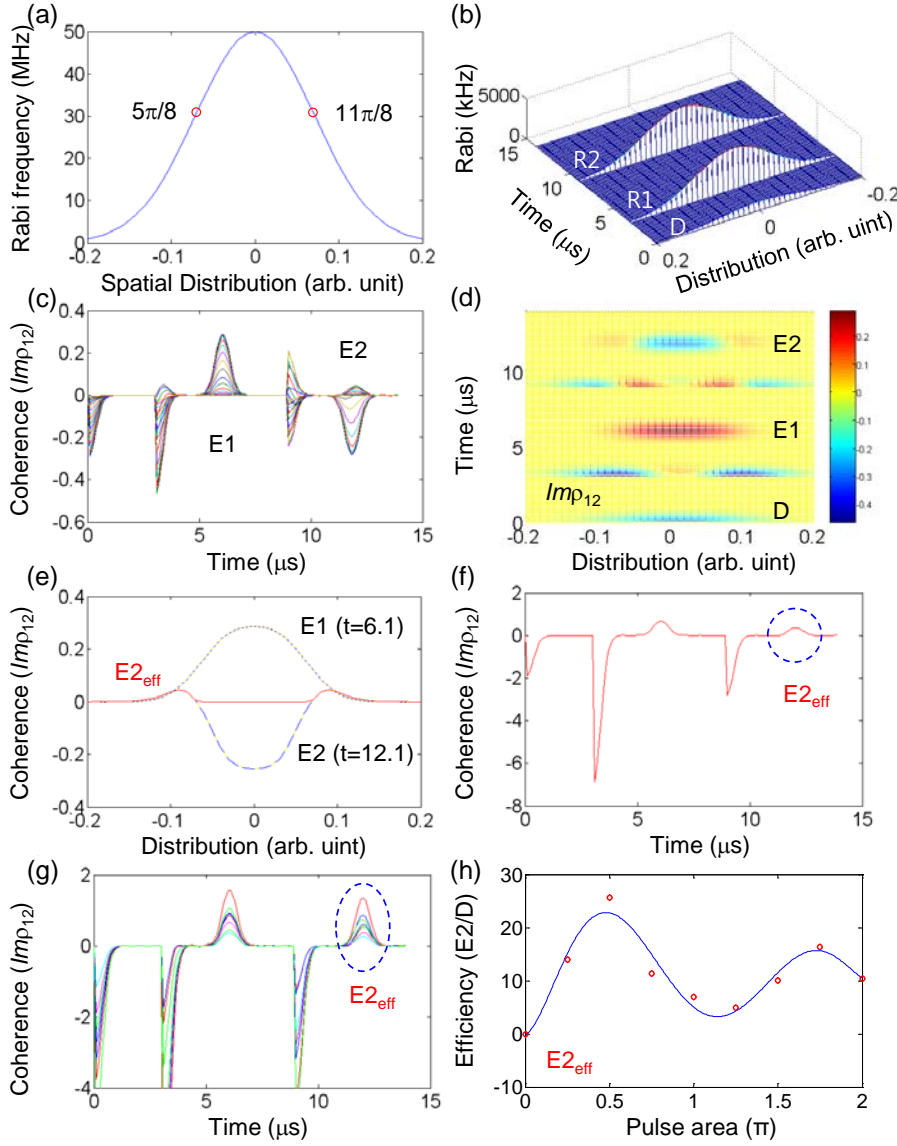
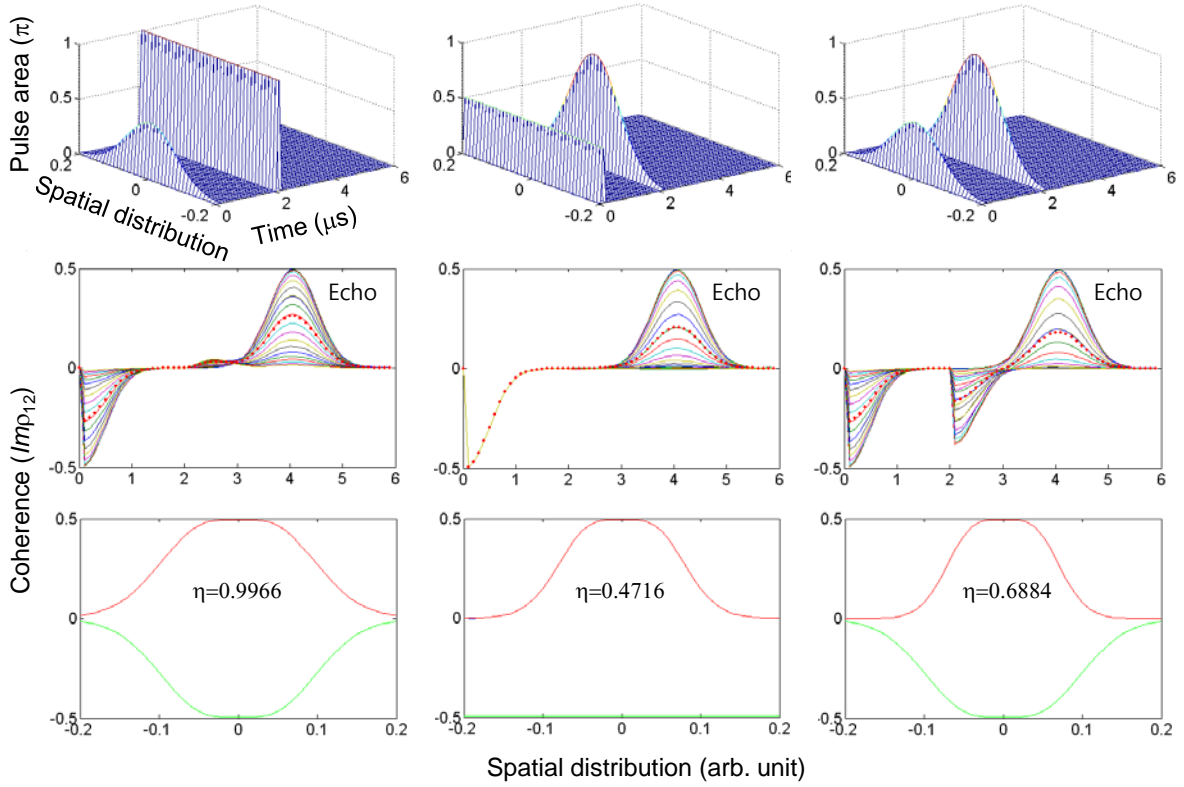
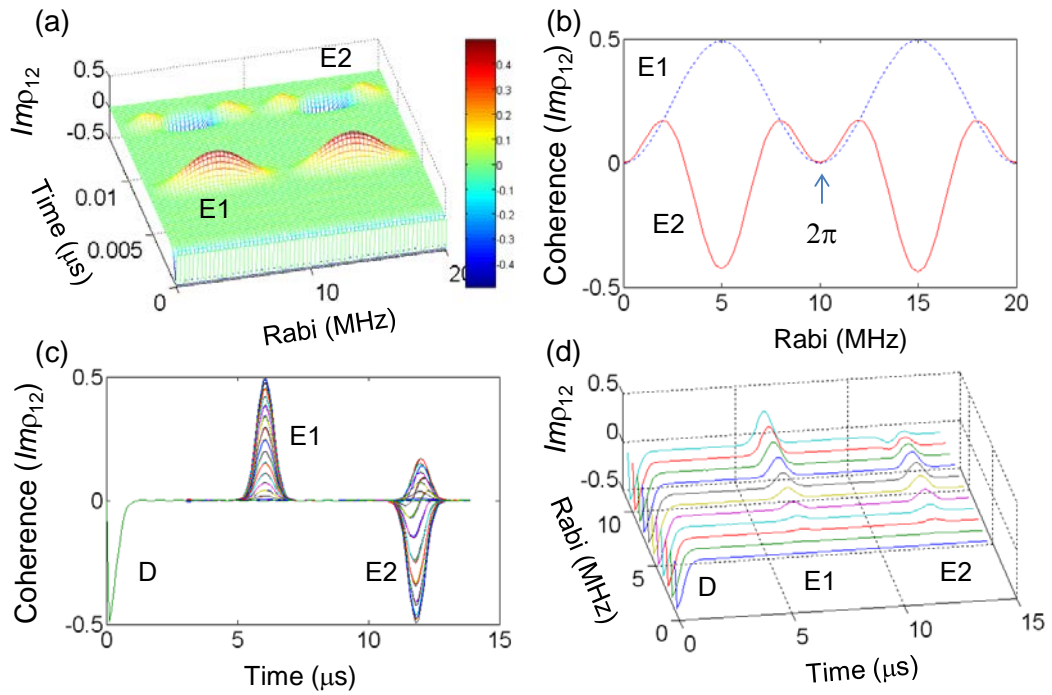


Figure 3. Gaussian spatial profile dependent photon echo efficiency in a double rephasing scheme. (a) Gaussian spatial profile. Red circles indicate the pulse area satisfying Eq. (2). (b) Pulse sequence for a double rephasing scheme. Data pulse area is set at  $\pi/5$  and others are  $\pi$  at peak power. The arrival time of Data D, Rephasing R1, and R2 is 0.1, 3.1, and 9.1  $\mu\text{s}$ , respectively. The Gaussian profile of (a) is divided into 41 parts at 10 kHz spacing, and each one is applied to the Rabi frequency of the rephasing pulses in (b). The data pulse area is not varied. (c) Individual coherence  $\rho_{12}$  for varied Rabi frequency. (d) A 2D picture of (c). (e) Coherence  $\rho_{12}$  as a function of Gaussian profile. The red curve is for  $\rho_{12} > 0$ . (f) Sum coherence  $\rho_{12}$  for  $E2_{\text{eff}}$  in (e). (g) Sum coherence  $\rho_{12}$  for different rephasing pulse area. Green:  $\pi/4$ ; Red:  $\pi/2$ ; Blue:  $3\pi/4$ ; Magenta:  $\pi$ ; Cyan:  $5\pi/4$ ; Green:  $3\pi/2$ ; Blue:  $7\pi/4$ ; Red:  $2\pi$ . (h) Red circle: peak amplitude ratio of echo e2 to the data in (g). Blue line: best-fit curve. The ratio  $E2_{\text{eff}}/D$  is with respect to the original data sum in (b).

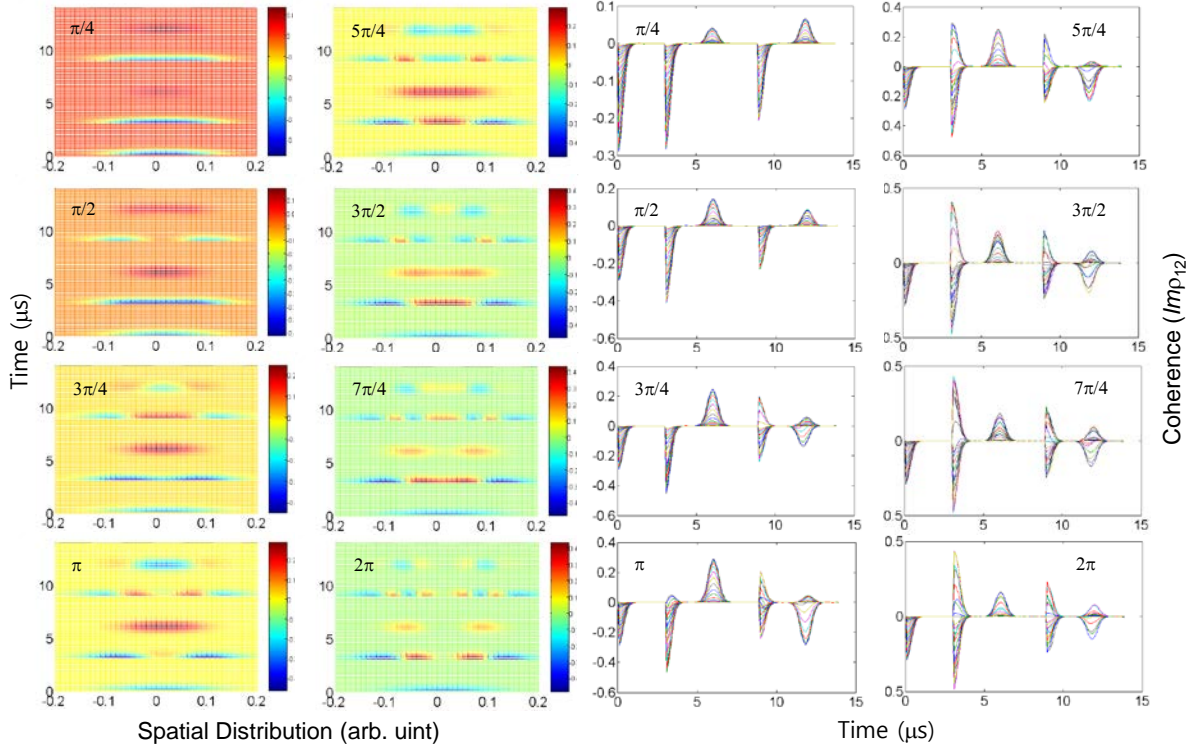
## Supplementary Information



Supplementary Figure 1. Gaussian spatial profile dependent photon echo efficiency in a single Raman scheme. First row: Pulse sequence for three different cases; Second row: Coherence evolutions for the spatially distributed components in the first row. The dotted curve is for average; Third row: Echo efficiency for the distributed components in the first row. The upper (lower) curve is for echo (data) at maximum along the distribution in the first row.



Supplementary Figure 2. Gaussian spatial profile dependent photon echo efficiency in a double rephasing scheme. (a) Coherence evolution of Fig. 2(a) vs. rephasing Rabi frequency. 10MHz corresponds to  $2\pi$  pulse area. (b) 1<sup>st</sup> (E1) and 2<sup>nd</sup> (E2) echoes vs. rephasing Rabi frequency. (c) and (d) Individual coherence evolutions of (a). All parameters are the same as those in Fig. 2, otherwise specified.



Supplementary Figure 3. Gaussian spatial profile dependent photon echo efficiency in a double raphaisng scheme. 1<sup>st</sup> and 2<sup>nd</sup> columns represent optical coherence ( $Imp_{12}$ ) as functions of time and spatial distribution for different pulse area ( $\pi/4 \sim 2\pi$ ) of rephasing pulses. 3<sup>rd</sup> and 4<sup>th</sup> columns represent individual optical coherences  $Im(Imp_{12})$  corresponding to the 1<sup>st</sup> and 2<sup>nd</sup> columns.